

Numerical and Experimental Study on the Properties of Laser Cladding of 6061Al Alloy

Chengyu Song¹ · Wenyu Wang² · Zhiqiang Ren² · Yang Zhao² · Li Zhou¹

Received: 24 October 2021 / Accepted: 22 November 2021 / Published online: 28 January 2022
© The Indian Institute of Metals - IIM 2021

Abstract A thermo-mechanical coupling model of laser cladding of AlSi10Mg powder on 6061Al alloy surface was established, and the influences of laser scanning speed (LSS) and power on residual stress and molten pool size were further discussed. The predicted properties of the model for laser cladding layer (LCL) simulation were verified by experiments on 6061Al alloy. The results show that the residual stress increases with increasing LSS and laser power. When the LSS is 6 mm/s and the power is 3600 W, the residual tensile stress is the lowest. In addition, due to the higher residual tensile stress on both sides of the LCL, the cracks occur easily. Moreover, only a few pores appear at the bonding surface of the LCL and the substrate.

Keywords Laser cladding · Double ellipsoid heat source · Laser cladding layer · Thermo-mechanical coupling

1 Introduction

6061Al alloy has comprehensive properties such as corrosion resistance, easy processing and fatigue resistance and is widely used as the main material in high-speed trains, automobiles and other fields [1, 2]. Owing to the

complex and changeable working environment, the surface of 6061 aluminum alloy parts is easily damaged. In addition, the manufacturing and scrapping costs of parts are relatively high, and then [3], repairing the damaged parts by laser cladding has become the research object of more and more scholars.

In the laser cladding process, the cladding effect is directly affected by the quality of the LCL. In the research of processing parameters on the geometry of the LCL, many scholars use simulation software to analyze the influence law. Hao et al. [4] studied the influence of different process parameters on the geometry of the Ti6Al4V alloy LCL. Luo et al. [5] established that a three-dimensional synchronous powder feeding model can analyze the influence of power and LSS on the size of the P20 substrate molten pool. Li et al. [6] analyzed the quality of 718 alloy LCL by the highest temperature, depth, dilution rate and forming factor. Gao et al. [7] analyzed the influence of process parameters on the shape and size of 316 stainless steel LCL and concluded that with the increase of LSS, the height and width of the molten pool decrease correspondingly. Liu et al. [8] used Gaussian heat source to simulate the laser cladding process, which can effectively predict the change of 5025Al alloy LCL geometry.

The existence of cracks in the LCL also has an important impact on the surface quality, and excessive tensile residual stress is the main reason for cracks. In the study of the residual stress distribution of the LCL, some scholars have used finite element analysis software to simulate the residual stress distribution. Dong et al. [9] used MSC/NASTRAN finite element analysis software to simulate the residual temperature stress of the LCL section. Guo et al. [10] analyzed the influence of input power and energy density on the stress distribution on the surface of the LCL. It is found that with the increase of input energy density,

✉ Li Zhou
lizhou@ytu.edu.cn

Yang Zhao
zhaoyang033@163.com

¹ School of Electromechanical and Automotive Engineering, Yantai University, Yantai 264005, China

² National Key Laboratory for Remanufacturing, Army Academy of Armored Forces, Beijing 100072, China

the tendency of center cracking decreases, and the tendency of edge cracking increases. Song et al. [11] studied the influence of the pattern, angle and length of the LCL as well as different coating methods on the residual stress. Wu et al. [12] studied the residual stress distribution of Ti–6Al–4V alloy and Inconel 718 in three different modes.

Up to now, there are few reports about laser cladding repair methods for 6000 series aluminum alloys. Most 6000 series aluminum alloys produce new surface properties through surface alloying and deposition of the metal surface [13, 14]. 6061 aluminum alloy is relatively common in 6000 series, but there is no report about AlSi10Mg powder cladding on 6061 substrates [15]. In this paper, a research method combining simulation and experiment was used to discuss the influence of LSS and power on the size, residual stress and maximum temperature of the 6061Al alloy substrate LCL.

2 Finite Element Analysis

2.1 Material Properties

When the mobile heat source acts on the surface of the metal powder, AlSi10Mg undergoes a process of transformation from a powder state to a molten state and finally solidifying. AlSi10Mg has different physical properties in different state. The density formula of powder is [16]:

$$\rho = \varphi\rho_g + (1 - \varphi)\rho_s \quad (1)$$

where φ is the porosity of the powder, ρ_g (kg/m^3) is the gas density, and ρ_s (kg/m^3) is the density of the AlSi10Mg alloy. Therefore, at room temperature (25 °C), the density of AlSi10Mg powder i has been calculated to be 1599 kg/m^3 (Table 1).

The thermophysical properties of the material are essential and important parameters in the temperature field. The specific heat, density and temperature conductivity of the material determine the shape of the LCL [4]. Due to the sequential temperature-mechanical coupling calculation method used in this article, the calculation results of the temperature field have a direct impact on the stress field. Figure 1 shows the related thermophysical parameters of AlSi10Mg powder and 6061 aluminum alloy [17].

2.2 Model Geometry and Mesh

ABAQUS finite element software is used to solve the calculation. 6061Al alloy substrate used in the experiment is 15 mm × 45 mm × 10 mm, and the thickness of the preset AlSi10Mg powder is 0.5 mm. The grid division and model are shown in Fig. 2. Considering the computational efficiency, the mesh transition technology is adopted. The grid uses an eight-node linear heat transfer hexahedral element (DC3D8). The temperature calculation step uses a heat transfer unit, and the mechanics calculation step uses a reduced mechanical unit. In order to simulate the stress and temperature fields more accurately when dividing the grid, the laser cladding area is divided into smaller grids, the grid size of the powder layer is 0.5 mm × 0.5 mm × 0.062 mm, and the grid size near the powder layer matrix is 1.5 mm × 1.5 mm × 0.2 mm. The grid size far away from the cladding zone is larger, the e size is 1.5 mm × 1.5 mm × 1.4 mm. The laser cladding area is divided into smaller grid sizes, and the grid size far away from the cladding area is larger, and the grid is relatively sparse. The large and small grid transition area adopts the transition method of grid number “3 to 1” [18].

2.3 Boundary Conditions

Boundary conditions are an indispensable and important part of the heat conduction finite element analysis model. The boundary conditions include initial conditions, displacement constraints and surface heat transfer conditions [18]. The initial condition is the ambient temperature of 20 °C. In the process of laser cladding, temperature convection and temperature radiation are the two main forms of heat loss. The equations of convection heat dissipation and radiation heat dissipation are expressed as [19]:

$$q_c = -h_c(T_s - T_0) \quad (2)$$

$$q_r = -\varepsilon\sigma \left[(T_s + 273.15)^4 - (T_0 + 273.15)^4 \right] \quad (3)$$

where h_c is the heat convective coefficient, T_s is the surface temperature of the LCL, T_0 is the ambient temperature of 293 K, ε is the surface thermal radiation of the substrate, σ is the boltzmann constant, which is $5.67 \times 10^{(-8)} \text{ W}/(\text{m}^2 \cdot \text{K}^4)$.

Table 1 6061 aluminum alloy chemical composition (mass fraction/%) [12]

Mg	Zn	Cu	Ti	Fe	Si	Mn	Al
0.96	0.0089	0.3	0.15	0.38	0.7	0.06	Balance

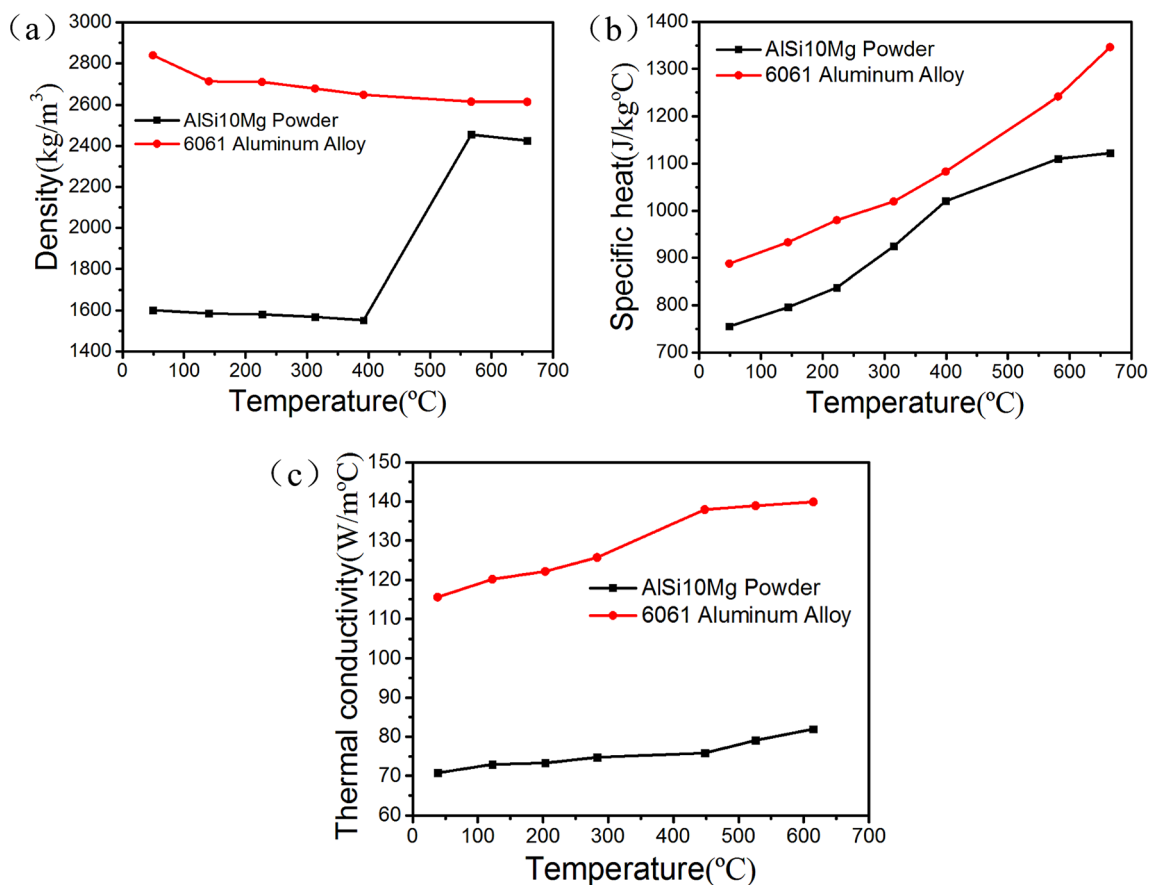


Fig. 1 Material properties: a density; b specific heat; c thermal conductivity

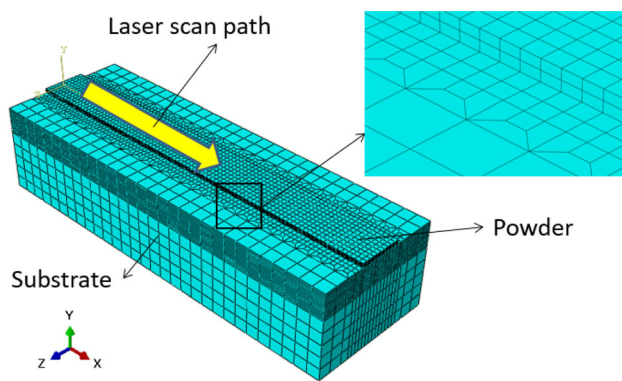


Fig. 2 Finite element model and mesh transition technology

2.4 Selection of Heat Source Model

The choice of heat input is important to the influence of the cladding temperature field and stress field. Different heat sources and spot parameters will cause different molten pool sizes and morphologies. However, as there is no equation that can completely fit the size of the molten pool so far, a large number of simulation experiments can only

be used to fit the molten pool to obtain more accurate heat source parameters.

The experiment uses a semiconductor output laser and a powder feeder to realize ring powder feeding or multi-beam powder feeding around the beam. A dedicated protective air duct has been set up, where the powder feeding beam, the beam and the protective air flow intersect at one point. This article uses a double ellipsoid model. Compared with Gaussian heat source, this heat source can simulate heat input more realistically. The double ellipsoid model equation is expressed as [20]:

The volume heat flux distribution of the first half of the model:

$$q(x, y, z) = \frac{6\sqrt{3}f_r q_0}{abc_f \pi \sqrt{\pi}} \exp\left(-\frac{3x^2}{c_f^2} - \frac{3y^2}{a^2} - \frac{3z^2}{b^2}\right) \quad (4)$$

The volume heat flux distribution of the second half of the model:

$$q(x, y, z) = \frac{6\sqrt{3}f_b q_0}{abc_b \pi \sqrt{\pi}} \exp\left(-\frac{3x^2}{c_b^2} - \frac{3y^2}{a^2} - \frac{3z^2}{b^2}\right) \quad (5)$$

where f_f and f_b are the heat source distribution coefficients of the front and back ellipsoid, $f_f + f_b = 2$; a , b , c_f , c_b are the shape parameters of the ellipsoid.

3 Results and Discussion

3.1 Temperature Field

In order to facilitate the description of the temperature–time curve of different nodes on the LCL, six temperature monitoring points have been set on the surface of the LCL, and the adjacent nodes have the same distance, as shown in Fig. 3a.

Figure 3b shows the historical temperature curves of 6 nodes selected along the scanning direction of the moving heat source when the LSS is 6 mm/s and the power is 4800 W. The figure can tell us that the temperature and time history of A, B, C, D, E and F are similar. Only the peak temperature and the peak time are different. After point C, the input energy is stable, the peak temperature of

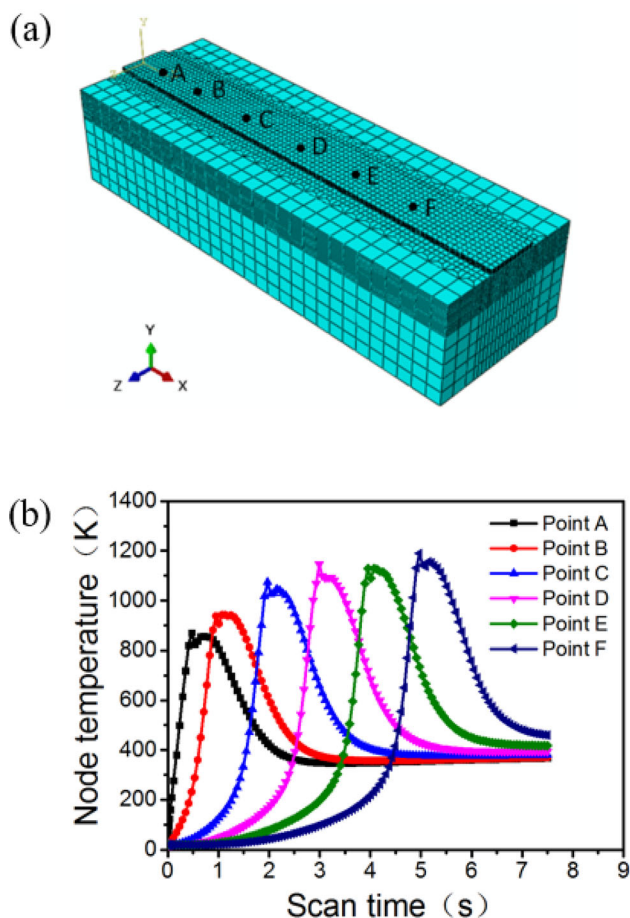


Fig. 3 Steady state interval: **a** temperature monitoring point; **b** temperature curve

the molten pool does not change, and the system temperature enters a steady state.

In order to study the influence of different process parameters on the temperature of the molten pool during the laser cladding process, a comparative study was carried out using the method of controlling variables. Keeping the LSS constant at 6 mm/s, the power is 3600 W, 4000 W, 4400 W, 4800 W, and the temperature field is compared, as shown in Fig. 4a–d. This group of pictures shows the temperature field when the time analysis step is 4.3 s. It can be seen from the figure that the power and temperature have a linear growth trend, that is, the temperature of the molten pool increases with the increase of power. When the power is 4800 W, the corresponding temperature is the highest, which is 1183 °C. When the laser power is 3600 W, the corresponding temperature is the lowest, which is 855 °C. This is because the higher the power, the more heat absorbed per unit area of the substrate surface, and the higher the temperature.

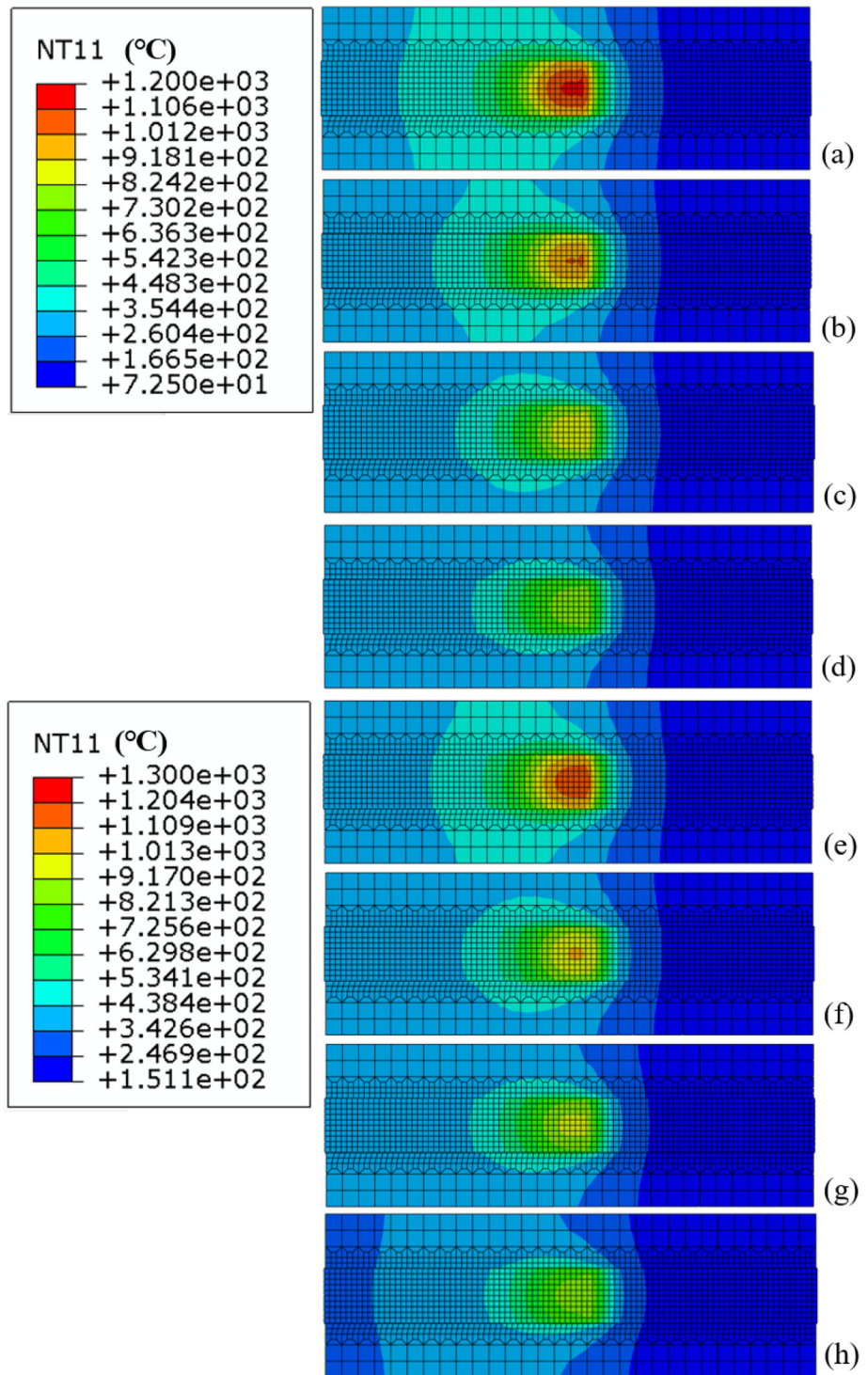
The power is kept constant at 4400 W and LSS at 4 mm/s, 6 mm/s, 8 mm/s and 10 mm/s, respectively, for comparative study, as shown in Fig. 4e–h. Due to the difference in LSS, each parameter has a different time analysis step. In order to ensure that the measurement results are obtained within the steady-state temperature range, there is no guarantee that the comparison can be performed at the same time analysis step. The graph can tell us that there is a negative growth trend between the maximum temperature and LSS. The maximum temperature decreases as the LSS increases. When the traverse speed is 4 mm/s, the temperature is the highest at 1254 °C. When the LSS is 10 mm/s, the temperature is the lowest at 839.4 °C. This is because the LSS increases, the heat transfer time between the heat source and the substrate surface decreases, the heat absorbed by the substrate decreases, and the final temperature decreases.

3.2 Molten Pool

Figure 5 is a comparison between the measured and the simulated molten pool, where H is the depth of the molten pool, and W is the width of the molten pool. The figure can tell us that the simulated size and morphology are identical with the experimental results.

Table 2 shows the comparison between the simulated and experimental molten pool sizes. Table 2 can tell us that the error is the smallest when the power is 4800 W, and the error of the depth and width is within 10%. Therefore, it can be concluded that the selected heat source model and its parameters are correct. The reason for the error is that, the material properties under high temperature conditions are difficult to obtain and can only be calculated by simulation, resulting in unavoidable errors [21]. Therefore, if

Fig. 4 Temperature field under different process parameters: **a** 4800 W 6 mm/s; **b** 4400 W 6 mm/s; **c** 4000 W 6 mm/s; **d** 3600 W 6 mm/s; **e** 4400 W 4 mm/s; **f** 4400 W 6 mm/s; **g** 4400 W 8 mm/s; **h** 4400 W 10 mm/s



the error exists and is within 10%, it can be considered that the heat source parameters are adequate.

The morphology of the molten pool obtained from the experiment is shown in Fig. 6. Figure 6a–d shows the morphology of the molten pool under different powers with a constant LSS. It can be seen from the figure that when the laser power is 3600 W, the width and height of the molten

pool are the smallest, 3.86 mm and 0.49 mm, respectively. When the laser power is 4800, the width and height of the molten pool are the largest, 4.57 mm and 1.12 mm, respectively. As the power increases, the height and width of the molten pool will increase. This is because the higher the laser power, the more heat absorbed per unit area, and the substrate material will also melt, resulting in a larger

Fig. 5 Comparison of simulated molten pool and measured molten pool

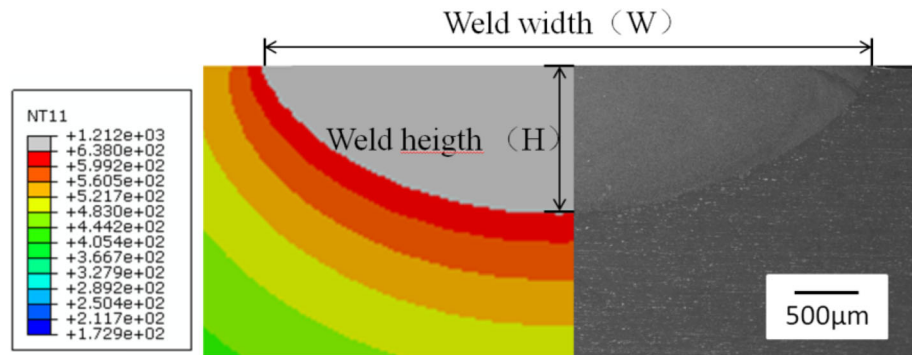


Table 2 Molten pool size comparison between simulated and experimental

Laser power/W	Experiment		Simulation		Error	
	W/mm	H/mm	W/mm	H/mm	W/%	H/%
3600	3.86	0.49	4.03	0.47	4.4	4.08
4000	4.23	0.94	4.36	0.86	3.07	8.5
4400	4.42	1.12	4.51	1.18	2.03	5.35
4800	4.72	1.25	4.62	1.21	2.11	3.2

molten pool. However, when the temperature is too high, more substrate material will enter the molten pool, which will also cause the dilution rate (LCL height/full height) to increase, and the increase in the dilution rate will reduce the quality of the performance coating. When the power is 3600 W, the dilution rate is the smallest.

Figure 6e–h shows the morphology of the molten pool under different LSSs with constant power. It can be seen from the figure that when the LSS is 10 mm/s, the width and depth of the molten pool are the smallest, which are 3.74 mm and 0.41 mm, respectively. When the LSS is 4 mm/s, the molten pool width and melting depth are the largest, 5.09 mm and 1.62 mm, respectively. The depth and width of the molten pool decrease as the LSS increases. This is because as the LSS increases, the heat transfer time between the heat source and the substrate decreases, the temperature decreases, and the melting amount of the substrate decreases, which in turn leads to a decrease in the molten pool.

The experimental and simulation results are compared, as shown in Fig. 7. The graph can tell us that the experimental and calculated results have the same trend under different powers and LSS. As the power increases, the depth and width of the molten pool increase. As the LSS increases, the depth and width of the molten pool decrease. Moreover, the results of the two are not much different, which can further verify the correctness of the model.

3.3 Residual Stress

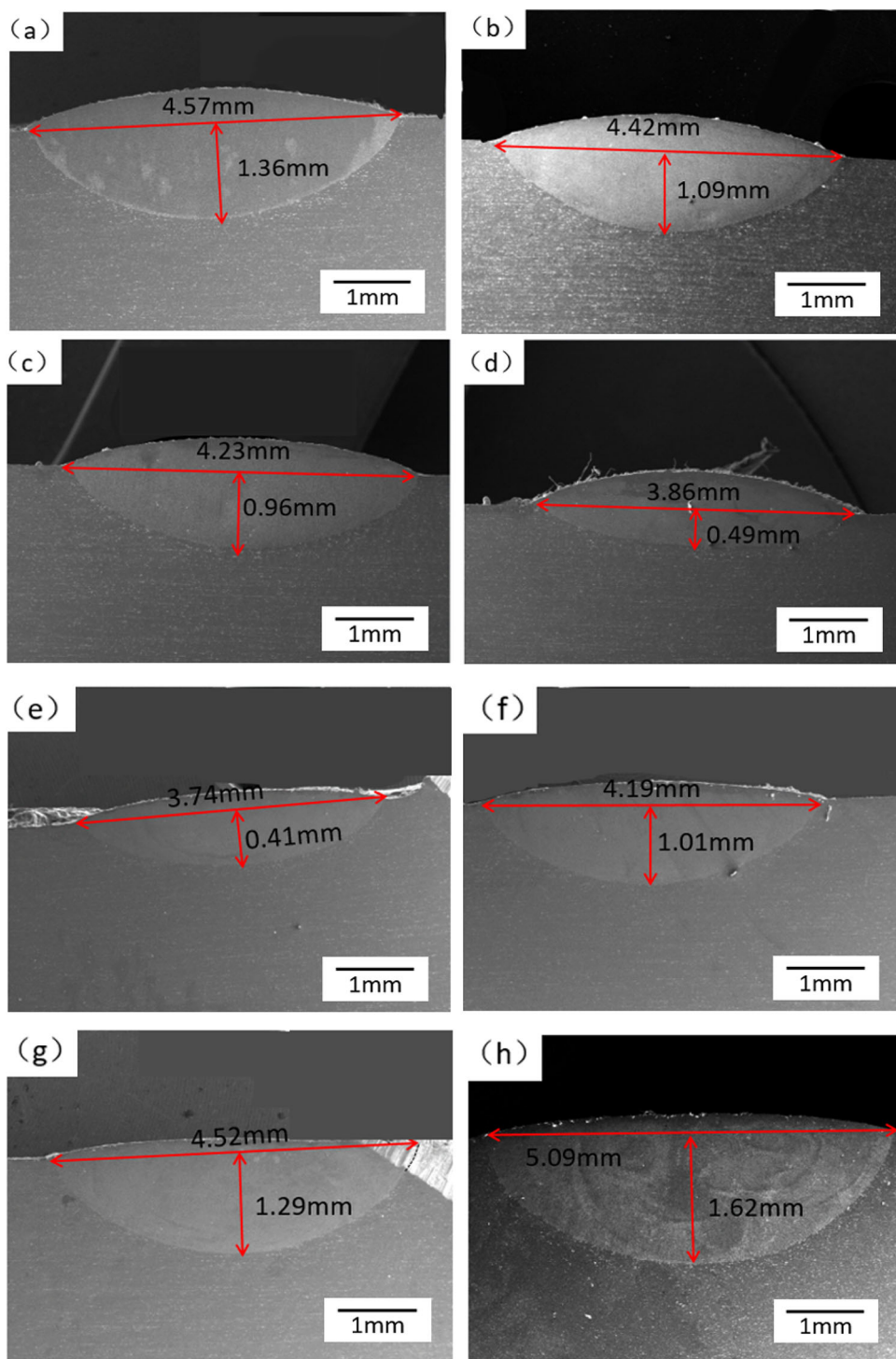
The model adopts sequential thermo-mechanical coupling calculation method. The DFLUX subroutine interface of the ABAQUS software is used to add a double ellipsoid heat source model to solve the temperature field. Then the calculation result of the temperature field is applied to the stress field as a load [22]. This calculation method is more efficient, and the temperature field has a unidirectional effect on the stress field, so the model can use sequential coupling.

3.3.1 The Influence of Different Processing Parameters on Residual Stress

In order to calculate the residual stress under different processing parameters more accurately, multiple paths are used, and the average value is used for comparison. This value method avoids the particularity of the selected section, and selects three sections in the steady-state interval to ensure a more accurate residual stress distribution. Then three paths on each section are selected. Comparing the average values of the above nine paths can more truly reflect the residual stress under different processing parameters.

In order to study the influence of different processing parameters on the residual stress after cladding. Figure 8a is a graph with the same LSS and laser powers of 4800 W, 4400 W, 4000 W and 3600 W. To ensure the accuracy of the data, the above-mentioned value method has been used

Fig. 6 Molten pool morphology under different process parameters, **a** 4800 W 6 mm/s; **b** 4400 W 6 mm/s; **c** 4000 W 6 mm/s; **d** 3600 W 6 mm/s; **e** 4400 W 10 mm/s; **f** 4400 W 8 mm/s; **g** 4400 W 6 mm/s; **h** 4400 W 4 mm/s



to measure the residual stress value. The graph shows that the residual stress increases with increasing power. When the laser power is 3600 W, the corresponding residual stress is the smallest. This is because as the power increases, the temperature and temperature gradient of the LCL will increase. The residual stress will increase as the temperature gradient increases. In addition, higher laser

power will also bring more energy, and the molten pool will also become larger. During the solidification process, the volume shrinkage of LCL will also increase, which will eventually lead to an increase in stress.

Figure 8b is a graph with constant power and scanning speeds of 4 mm/s, 6 mm/s, 8 mm/s and 10 mm/s. This figure shows that as the LSS increases, the tensile residual

Fig. 7 Comparison of experimental and simulated molten pool size vs processing parameters: **a**, **b** laser power; **c**, **d** LSS

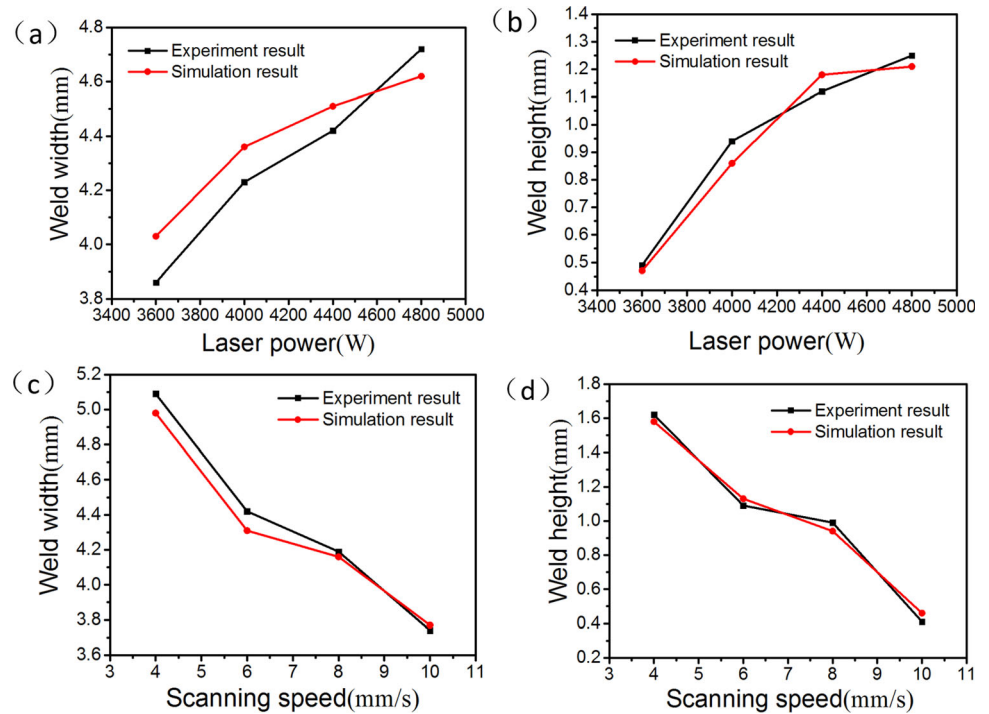
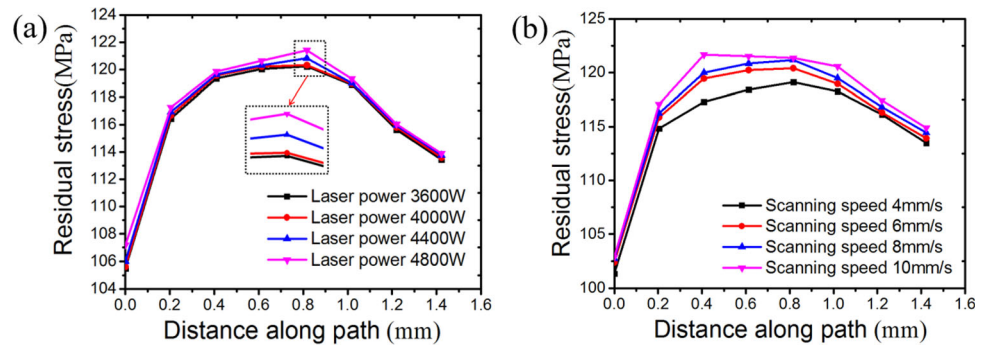


Fig. 8 Residual stress under different parameters: **a** laser power; **b** LSS



stress becomes larger. This is because when the LSS increases, the energy absorbed by the powder surface decreases and the cooling rate increases. The melting and cooling of the solidified layer material become more intense, causing the material to retain more plastic deformation on the LCL. LCL affects the increase of residual stress [23]. When LSS is 4 mm/s and 6 mm/s, the residual stress is smaller. But if the LSS is too low, it is easy to cause pores in the LCL, so the best LSS is 6 mm/s.

3.3.2 Residual Stress Distribution

The residual stress distribution in the S33 direction is shown in Fig. 9a. The figure can tell us that in the steady state interval, the tensile residual stress is mainly distributed on both sides of the LCL. It can also be seen from the A-A cross-sectional view that stress concentration areas also appear on both sides of the LCL, with a tensile stress

of 155 MPa. We know that the tensile strength of 6061 aluminum alloy is 112 MPa [24]. It can be predicted that cracks are prone to appear on both sides of the LCL.

The distribution of cracks in the LCL in the experiment, is shown in Fig. 9b. It can be found that the cracks are mainly concentrated in the areas on both sides of the LCL. They are formed from the inside of the LCL and extend into the inside of the substrate. However, no cracks are found at the bottom of the LCL, which is similar to the numerical simulation results. At the same time, it also illustrates the predictive effect of the model on the location of cracks.

3.4 Production of Porosity

The pores are actually bubble in the liquid metal, which fail to escape in time during the cooling process of the liquid metal. As a result, microscopic defects are formed in the

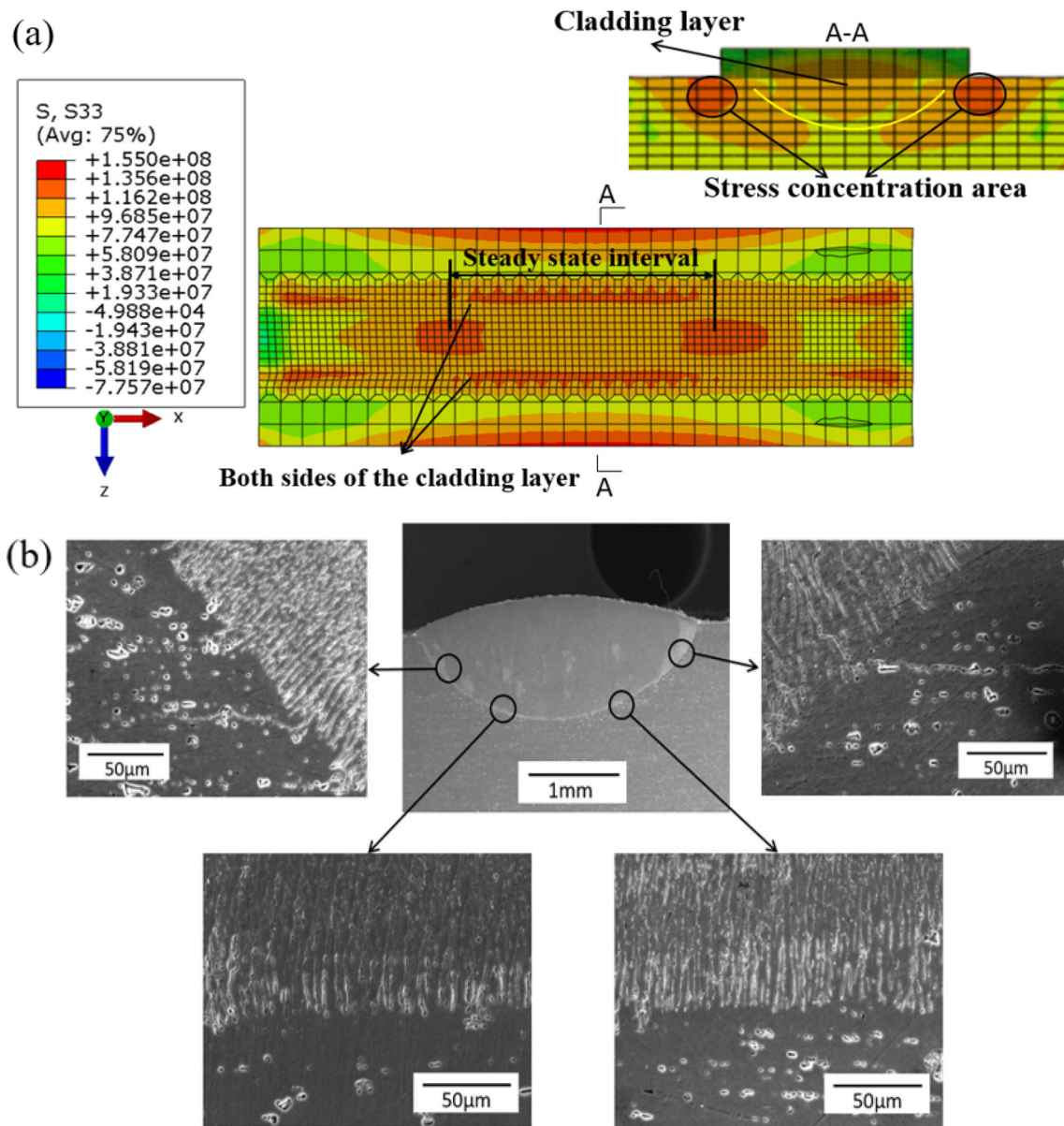


Fig. 9 Residual stress distribution: **a** stress cloud; **b** crack distribution in the LCL

metal structure, as shown in Fig. 10a. The existence of pores not only affects the compactness of the LCL, but also affects the anti-corrosion ability of the coating of the LCL. At the same time, the parts with pores are more prone to stress concentration, inducing to the generation of micro-cracks [25]. Power and LSS are important agents that affect the formation of stomata. When the LSS is lower and the power is higher, the action time between the powder and the laser becomes longer. The more the substrate melts, the larger the molten pool size. The increased fluidity of the liquid will cause more gas to be sucked into the molten pool and cannot overflow in time. As a result, air holes are formed, as shown in Fig. 10b, for a schematic diagram of air hole formation.

4 Conclusions

In this paper, a sequential thermo-mechanical coupling calculation method is used to establish a simulation model. The influence law of the stress field and temperature field of the LCL under process parameters is analyzed, and the distribution law of the tensile residual stress of the LCL is studied. Through comparison, the reasons for the formation of pores in the LCL are discussed. Can be summarized as follows:

1. The size and temperature of the molten pool decrease as the LSS increases, but the residual stress is reversed. The size, maximum temperature and residual stress of

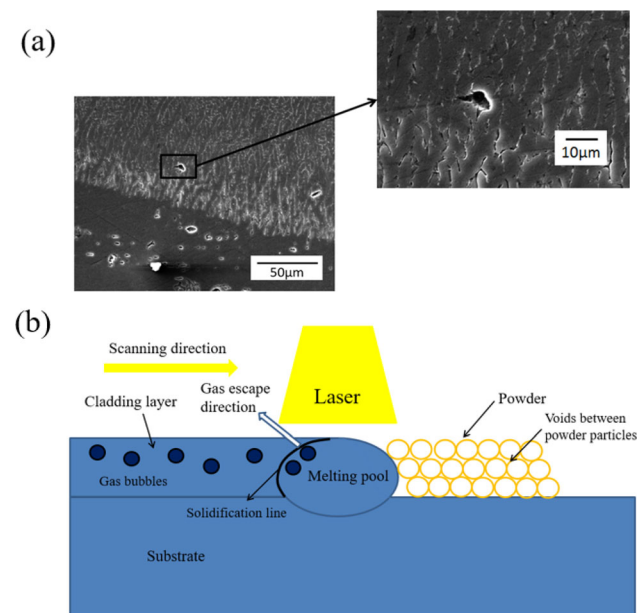


Fig. 10 Production of porosity: **a** porosity in the LCL; **b** diagrammatic drawing of the existence of pores

the LCL increase with the increase of power. When the laser power is 3600 W and the LSS is 6 mm/s, the residual stress is the smallest and the number of cracks is the smallest, that is, the best cladding effect is produced.

- By setting temperature monitoring points on the scanning path, the constant temperature range of the processing process is obtained. The numerical results of the shape of the molten pool are identical with the experimental results of 6061Al alloy, and the error is less than 10%.
- Through simulation and experimental observation, the areas with greater stress are mainly concentrated on both sides of the LCL. The pores actually evolve from bubbles that fail to escape in time during the cooling process of the liquid metal and mainly appear near the junction of the melting zone and the substrate.
- The model in this paper has a good crack prediction effect, that is, the location of the crack can be roughly inferred from the residual stress model.

Funding National Key R&D Program of China, 2018YFB1105800.

References

- Priya R, Subramanya Sarma V, and Prasad Rao K, *T Indian I Metals* **62** (2009) 11.
- Rouniyar A K, and Shandilya P, *Part I Mech Eng C-J Mec* **235** (2021) 1.
- Zhang J, Zong X W, Chen Z, and Fu H G, *T Indian I Metals* (2021) 1.
- Hao M Z, and Sun Y W, *Int J Heat Mass Tran* **64** (2013) 352.
- Luo F, Yao J H, and Hu X X, *J Iron Steel Res Int* **18** (2011) 73
- Li Y M, Yao D Z, and Fan F J, *Applied Laser* **38** (2018) 920.
- Gao J L, Wu C Z, and Hao Y B, *OPT Laser Technol* **129** (2020) 106287.
- Liu C M, Li C G, and Zhang Z, *OPT Laser Technol* **123** (2020) 105926.
- Dong S Y, Xu B S, and Liang X B, *China Surf En* **14** (2001) 15.
- Guo X G, Huang J, and Zhou Z, *J Therm Spray Technol* **12** (2020) 12.
- Song M J, Wu L S, and Liu J M, *OPT Laser Technol* **133** (2021) 106531.
- Wu Q R, Mukherjee T H, and Liu C M, *Addit Manuf* **29** (2019) 100808.
- Man H C, Yang Y Q, and Lee W B, *Surf Coat Technol* **185** (2004) 74.
- Man H C, Zhang S, and Cheng F T, *Mater Lett* **61** (2007) 4058.
- Ozturk F, Sisman A, and Toros S, *Mater Des* **31** (2009) 972.
- Gusarov A V, and Smurov I, *Physics Procedia* **5** (2021) 381.
- [Zhu S H, Shao S, and Yang H H, *Metalworking Magazine, Institute of Machinery Industry Information* **4** (2019) 709.
- Kang Y, Zhan X H, and Feng X S, *Aerospace Shanghai (Chinese & English)* **37** (2020) 58.
- Zhang T G, Zhang Q, and Yao B, *Laser & Optoelectronics Progress* **58** (2021) 220.
- Liu X Y, *Mechatronics Technol* **47** (2016) 51.
- Zhang Q M, Liu W J, and Zhong M L, *Metal Heat Treatment* **28** (2003) 11.
- Miao C H, Cao L J, and Yin K, *Light Industry Mach* **38** (2020) 46.
- Xiao Z X, Chen C P, and Zhu H H, *Materials & Design* **193** (2020) 108846.
- Yuan G S, and Yang Z Y, *Materials for Mech En* **42** (2018) 68.
- Zhang J H, and Sun R L, *Hot Processing Technol* **44** (2015) 141.

Publisher's Note Springer Nature remains neutral with regard to jurisdictional claims in published maps and institutional affiliations.